Theory of ultrasound propagation in $LuCo_3$ near the low-spin–high-spin crossover

A. A. Tereshchenko,[1] A. S. Ovchinnikov,[1,2] D. I. Gorbunov,[3] and D. S. Neznakhin[1]
[1]*Institute of Natural Science and Mathematics, Ural Federal University, Ekaterinburg 620002, Russia*
[2]*Institute of Metal Physics, Ural Division, Russian Academy of Sciences, Ekaterinburg 620219, Russia*
[3]*Hochfeld-Magnetlabor Dresden (HLD-EMFL), Helmholtz-Zentrum Dresden-Rossendorf, 01328 Dresden, Germany*

(Received 19 May 2022; accepted 4 August 2022; published 15 August 2022)

The possibility of experimental observation of the ultrasonic attenuation in the ferromagnet $LuCo_3$ near the low-spin-high-spin crossover is discussed. We show that ultrasound propagation gives rise to transitions between states of the magnon band due to absorption of phonons, and this process is highly sensitive to the value of magnetization. The high magnetic field, which governs the crossover, alters the ultrasound propagation regime from off-resonant to resonant and we formulate a criterion of the change. Calculated temperature and field dependences of the ultrasonic wave number and attenuation clearly demonstrate anomalies in these characteristics in the vicinity of the crossover at intermediate temperatures far below the Curie temperature.

DOI: 10.1103/PhysRevB.106.054417

I. INTRODUCTION

Magnetism of a large group of materials composed of $4f$ rare-earth (R) and $3d$ transition metal (T) ions, which are known as intermetallic compounds, is related to two principally different types of electrons. The $4f$ electrons are localized and provide a large magnetocrystalline anisotropy. Being partly itinerant, the $3d$ electrons are a source of strong exchange interactions due to their extended wave functions. The combination of the $3d$ and $4f$ electrons in intermetallic compounds makes it possible to achieve good hard magnetic properties favored in material design of permanent magnets [1–3]. According to the general rule, the spin moments of the ferromagnetic $3d$ elements T = Fe, Co, and Ni are aligned antiparallel to the spin moments of a rare earth [4]. This leads to ferrimagnetic order in the R-T compounds with the heavy rare-earth elements, R = Gd–Yb, where the $4f$ shell is half-filled, or more. By contrast, the R-T compounds with the light rare-earth elements, Pr–Sm, where the moment is mainly orbital in character and directed opposite to the spin moment according to Hund's rule, exhibit ferromagnetism.

The R-T ferrimagnets are of special interest for studies in high magnetic fields because they undergo field-induced magnetic phase transitions when the applied field starts to compete with the exchange and anisotropy interaction [5–8]. Such transitions reflect breaking of the initial antiparallel alignment between the R and T moments due to spin reorientation of the $4f$ and $3d$ magnetic moments. Early mean-field studies of this magnetization process provide a wealth of useful information on the strength of the R-T intersublattice exchange coupling and magnetocrystalline anisotropy [9–11].

Being relatively uncommon, field-induced phase transitions in ferromagnets do occur and require special attention. One of them is $LuCo_3$, in which lutetium bears no ordered magnetic moment, was recently examined using magnetization measurements in pulsed magnetic fields up to 58 T. [12] A pronounced jump of magnetization was revealed just below 50 T for both easy and hard magnetization directions of the applied field, which suggests that the transition is of exchange origin. This conclusion has been supported by *ab initio* calculations based on the density functional theory, which show that the transition is due to a significant redistribution in the majority and minority spin states in the Co $3d$ subsystem [12].

Besides the microscopic origin of the transition, another important issue is a manifestation of this effect in different physical processes, particularly, in a response of lattice degrees of freedom. It is well recognized that relevant information about magnetic phase transitions may be gained from ultrasonic measurements because they can be fairly easily detected by the experimental technique [13,14]. Commonly used characteristics of propagation of ultrasonic waves are their velocity and attenuation dependent on magnetic properties of the solid. A variety of effective uses of ultrasonic methods for study of magnetic phase transitions characterized by Curie or Néel temperatures [15–18], first-order transition [19], and spin reorientation transitions [20–28] were reported.

Despite the remarkable progress, there remain a need for a theoretical analysis of details of ultrasound propagation near the low-spin-high-spin transition observed in $LuCo_3$. A particular feature of the effect is that it happens in very high magnetic fields far below the Curie temperature $T_C \approx 376$ K. [12] Similar transitions from low-spin to high-spin states have been observed in rare-earth intermetallic compounds such as YCo_3 [29], $Y(Co_{1-x}Fe_x)_3$ [30], YCo_5 and $LaCo_5$ [31,32], which also occur at temperatures below T_C as a function of magnetic field or pressure. In these circumstances, theoretical approaches developed to study the anomaly in sound wave attenuation and attendant frequency dispersion at the critical point [33–37] become inefficient. Indeed, the jump of magnetization in $LuCo_3$ is not accompanied by a change in symmetry, i.e., a situation of spin crossover arises at which nature of spin fluctuations does not alter qualitatively.

Another important aspect is linked to the ultrasound frequency range (∼100 MHz), which is far below characteristic frequencies of spin-wave excitations (∼1–10 THz) in the highly anisotropic magnet, like $LuCo_3$, shifted additionally upward by the high magnetic field. This rules out the resonant mechanism of magnetoelastic coupling between acoustic and spin waves [38,39].

However, these reasons do not preclude another way to transfer energy from phonons to spin subsystem, when ultrasound propagation causes intraband transitions between different one-magnon states. The energy difference between these states $\varepsilon_{\mathbf{q}+\mathbf{k}} - \varepsilon_{\mathbf{q}}$ is determined both by the wave vector $\mathbf{k}$ of the absorbed phonon and by the slope of the branch $\varepsilon_{\mathbf{q}}$ of magnon excitations. The latter is greatly affected by the magnetization, namely, the magnon branch is relatively flat in the low-spin state and becomes steeper in the high-spin state. In these circumstances, we show in this paper that no resonant phonon absorption occurs below the crossover, since the ultrasound energy $\hbar\omega_e$ exceeds the difference $\varepsilon_{\mathbf{q}+\mathbf{k}} - \varepsilon_{\mathbf{q}}$. However, the transition to the high-spin state makes the process feasible because of equalizing these two energies.

We also demonstrate that the probability of the process is proportional to the thermal population of magnon states. Therefore, ultrasound propagation through the specimen is unaffected at low temperatures since excitation of spin waves is strongly suppressed by the anisotropy and the external magnetic field. In contrast, the resonance phonon absorption may occur with high probability at intermediate temperatures that causes a large increase of the ultrasound attenuation together with a drastic variation of the ultrasound wave number (or velocity) near the crossover point.

Our analysis of ultrasonic attenuation uses the formalism suggested by Kwok [40] which allows for linear response of lattice vibrations to an external force by means of the diagrammatic phonon Green's function technique [41]. The latter has proved to be an effective tool for tackling problems regarding the magnon-phonon coupling in magnetic materials [42–44]. The interaction of the ultrasound waves with magnetic ions of $LuCo_3$ is treated within the exchange strain mechanism of spin-phonon coupling [45]. With this approach, a criterion of a change of the ultrasound propagation regime from off-resonant to resonant can be explicitly formulated.

The paper is organized as follows: In Sec. II we describe the model of spin and lattice excitations relevant for $LuCo_3$ and specify the mechanism of spin-phonon coupling. In Sec. III basic equations of ultrasound propagation in media are deduced with the aid of the retarded phonon Green's functions. In Sec. IV this approach is adopted in order to realize ultrasound absorption measurements in $LuCo_3$ for experimental verification. The predicted magnetic field and temperature dependences of the ultrasound attenuation coefficient and the ultrasound wave number are discussed in Sec. V. The conclusions are given in Sec. VI.

II. MODEL

The two-component intermetallic compound $LuCo_3$ has a trigonal crystal structure of $PuNi_3$ type (space group $R\bar{3}m$) with the lattice parameters $a = b = 4.956$ Å and $c = 24.126$ Å (see Fig. 1). The translation vectors of the trigonal (hexagonal) Bravais lattice are $\mathbf{a}_1 = (a, 0, 0)$, $\mathbf{a}_2 = (-a/2, \sqrt{3}a/2, 0)$ and $\mathbf{a}_3 = (0, 0, c)$. Throughout the present study we assume that these lattice parameters remain unchanged, i.e., any possibility of structural transitions [46] (including those associated with the external magnetic field) is excluded.

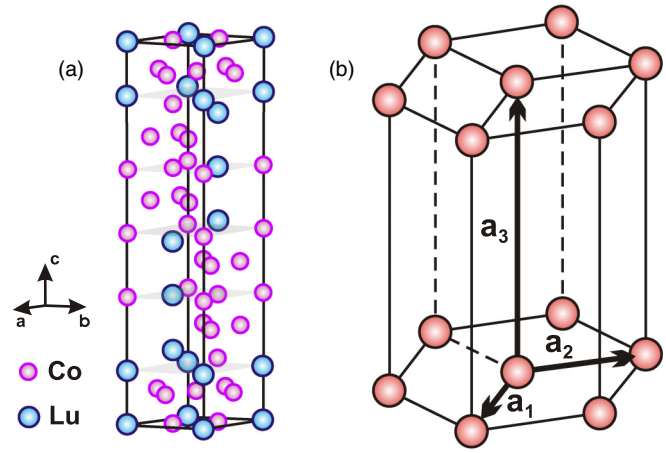

FIG. 1. Crystal structure of $LuCo_3$ (a) and the coarse-grained trigonal lattice with the sites (red balls) corresponding to the effective spin moment of the entire unit cell of $LuCo_3$ (b).

Ultrasonic measurements are directly related to excitation of acoustic phonon modes in solids when neighboring atoms oscillate almost perfectly in phase in the long-wave limit. Due to ferromagnetic alignment of the magnetic moments of individual ions in $LuCo_3$, it is plausible to assume that these acoustic modes will be coupled to the total magnetic moment of the elementary cell since the internal structure of the unit cell is irrelevant from the viewpoint of these vibrations. For this reason $LuCo_3$ can be pictured as a collection of pointlike atoms which form the trigonal Bravais-type lattice and each of the atoms has a mass and a magnetic moment of the entire unit cell of $LuCo_3$.

The effective spin per unit cell $S = 9M_S/g_S\mu_B$, where g factor ($g_S = 2$), μ_B is the Bohr magneton, and M_S is the saturation magnetization. The factor 9 appears because each unit cell contains this number of the formula units. $LuCo_3$ displays an uniaxial magnetic anisotropy and the spontaneous magnetic moment along the easy [001] axis is $M_S = 1.77\ \mu_B$/f.u. [12], which corresponds to $S \approx 7.97$. It is clear that the magnitude of the effective spin follows exactly the field dependence of the saturation magnetization (see Supplemental Material [47]).

Then, the magnon excitation spectrum can be derived from the effective model of Heisenberg ferromagnet on the trigonal Bravais-type lattice [see Fig. 1(b)] with the Hamiltonian

$$\mathcal{H}_m = -\sum_{i,j} J_{ij}\mathbf{S}_i\mathbf{S}_j - D\sum_i (S_i^z)^2 + g_S\mu_B\mu_0 H\sum_i S_i^z, \quad (1)$$

where the spin operators $\mathbf{S}_i$ are located at the sites $\mathbf{R}_i$ of the lattice and related with the coarse-grained magnetization $\mathbf{M}(\mathbf{r}) = g_S\mu_B\sum_i \mathbf{S}_i\delta(\mathbf{r} - \mathbf{R}_i)$. The first term describes ferromagnetic nearest-neighbor exchange coupling. The second term corresponds to single-ion easy-axis anisotropy, where the crystallographic c axis is the easy direction of magnetization.

The last term arises due to the external magnetic field $\mu_0 H$ applied along this direction (z axis). In our model treatment, we assume that only the effective spin S varies with the external magnetic field H in accordance with the magnetization data, while the Hamiltonian parameters, J_{ij} and D, remain unaffected by H.

Ferromagnetic exchange interaction between the nearest-neighbor sites in the basal ab-plane will be denoted as $J(a)$, and the notion $J(c)$ will be used for similar interaction between magnetic moments along the c-axis. Apparently, $J(a)$ is larger than $J(c)$ since $c > a$, but no precise values are available, so the ratio $J(a)/J(c) = 5.0$ is chosen in our numerical calculations to reduce the number of independent parameters. The value $J(a)$ is treated as a fitting parameter of the theory, but an order of the magnitude may be estimated from the Curie temperature $T_C \approx 376\,\mathrm{K}$ [12]. Given $J(a) \sim 3k_B T_C/2ZS(S+1)$, where $Z = 6$ is the number of the nearest neighbors in the ab plane, one gets $J(a)/k_B \sim 1.0\,\mathrm{K}$.

According to experimental data [12], the uniaxial crystal $LuCo_3$, having $n = 2/(\sqrt{3}a^2 c) \approx 1.949 \times 10^{27}$ elementary cells per m^3, possesses the effective anisotropy constant $K_1 \approx 1.571 \times 10^6\ \mathrm{J/m}^3$ that immediately yields [48]

$$D = K_1/(nS^2) \approx 1.269 \times 10^{-23}\,\mathrm{J}$$

for $S = 7.97$.

Because of the large spin quantum number, the spin operators may be represented by boson operators via the Holstein-Primakoff representation

$$S_i^+ = \sqrt{2S}\hat{a}_i^\dagger (1 - \hat{a}_i^\dagger \hat{a}_i/2S)^{\frac{1}{2}} \approx \sqrt{2S}\left[\hat{a}_i^\dagger - \frac{\hat{a}_i^\dagger \hat{a}_i^\dagger \hat{a}_i}{4S}\right],$$
$$S_i^- = \sqrt{2S}(1 - \hat{a}_i^\dagger \hat{a}_i/2S)^{\frac{1}{2}} \hat{a}_i \approx \sqrt{2S}\left[\hat{a}_i - \frac{\hat{a}_i^\dagger \hat{a}_i \hat{a}_i}{4S}\right], \quad (2)$$

$$S_i^z = -S + \hat{a}_i^\dagger \hat{a}_i,$$

where the square roots are expanded due to the large value of the effective spin S.

Substituting these into Eq. (1) and introducing the Fourier transform of the bose operators

$$\hat{a}_i = \frac{1}{\sqrt{N}} \sum_{\mathbf{q}} e^{i\mathbf{q}\mathbf{R}_i} \hat{a}_{\mathbf{q}}, \quad (3)$$

the magnetic Hamiltonian takes the simple form

$$\mathcal{H}_m = E_0 + \sum_{\mathbf{q}} \varepsilon_{\mathbf{q}} \hat{a}_{\mathbf{q}}^\dagger \hat{a}_{\mathbf{q}}, \quad (4)$$

where the terms quatric in the boson operators are neglected, since in our analysis no magnon-magnon interactions are accounted for. Here E_0 is the energy of the ferromagnetic ground state, and the excitation energy is given by

$$\varepsilon_{\mathbf{q}} = 2S[\tilde{J}(\mathbf{0}) - \tilde{J}(\mathbf{q})] + D(2S-1) + g_S \mu_B \mu_0 H \quad (5)$$

with

$$\tilde{J}(\mathbf{0}) = 2J(c) + 6J(a),$$

$$\tilde{J}(\mathbf{q}) = 2J(a)\left[\cos(q_x a) + 2\cos\left(\frac{1}{2}q_x a\right)\cos\left(\frac{\sqrt{3}}{2}q_y a\right)\right] + 2J(c)\cos(q_z c). \quad (6)$$

The energy contribution of lattice vibrations is given by

$$\mathcal{H}_p = \sum_{\mathbf{k}s} \hbar\omega_s(\mathbf{k})\left(\hat{b}_{\mathbf{k}s}^\dagger \hat{b}_{\mathbf{k}s} + \frac{1}{2}\right), \quad (7)$$

where $\hat{b}_{\mathbf{k}s}^\dagger$ ($\hat{b}_{\mathbf{k}s}$) are the creation (annihilation) operators, respectively, of a phonon of the wave vector $\mathbf{k}$ and the branch label $s = 1, 2, 3$, which increase (reduce) the energy by the amount $\hbar\omega_s(\mathbf{k})$.

The atomic displacements $\mathbf{u}_i = \mathbf{r}_i - \mathbf{R}_i$ of the i-th unit cell position $\mathbf{r}_i$ from the equilibrium position $\mathbf{R}_i$ are expressed in terms of these creation and annihilation operators as

$$u_i^\alpha = \sqrt{\frac{\hbar}{2mN}} \sum_{\mathbf{k}s} \frac{\mathbf{e}_\alpha(\mathbf{k}s)}{\sqrt{\omega_s(\mathbf{k})}} e^{i\mathbf{k}\mathbf{R}_i}(\hat{b}_{\mathbf{k}s} + \hat{b}_{-\mathbf{k}s}^\dagger), \quad (8)$$

where $\alpha = x, y, z$ and $\mathbf{e}_\alpha(\mathbf{k}s)$ is the polarization vector. The effective unit cell mass appearing in Eq. (8)

$$m = \frac{\sqrt{3}}{2}\rho a^2 c = 5.296 \times 10^{-24}\,\mathrm{kg},$$

where the mass density $\rho = 10.32\,\mathrm{g/cm}^3$ (see Ref. [12]). N is the number of the unit cells.

To describe interaction of strain waves with magnetic ions we use the Waller mechanism [13], when the strain wave modulates the distance between two magnetic ions, thus changing the exchange interaction

$$-\sum_{ij}[J(\mathbf{R}_{ij} + \mathbf{u}_i - \mathbf{u}_j) - J(\mathbf{R}_{ij})]\mathbf{S}_i\mathbf{S}_j, \quad (9)$$

where $\mathbf{R}_{ij} = \mathbf{R}_i - \mathbf{R}_j$ is the equilibrium distance between two magnetic ions. We note, that the alternative mechanism of the strain-single-ion coupling results from strain derivative of the crystal fields, or concomitant anisotropy energy in magnetically ordered media [49,50]. However, this approach is suitable for systems where d electrons in partially filled shells occupy well-localized ioniclike states, whereas partly itinerant d electrons in the metallic $LuCo_3$ participate in conduction [51].

By expanding Eq. (9) in the displacements $\mathbf{u}_i$, the spin-lattice interaction may be presented as [45,52]

$$\mathcal{H}_{mp} = -\sum_{i,\boldsymbol{\delta}}\left(\frac{1}{\delta}\frac{dJ}{d\delta}\right)([\mathbf{u}_{i+\boldsymbol{\delta}} - \mathbf{u}_i]\,\boldsymbol{\delta})(\mathbf{S}_{i+\boldsymbol{\delta}}\,\mathbf{S}_i), \quad (10)$$

where $\boldsymbol{\delta}$ is the distance between the nearest neighbors. Transforming, by means of Eqs. (2) and (8), this expression in terms of the creation and annihilation operators, one obtains

the exchange-mediated magnon-phonon interaction

$$\mathcal{H}_{mp} = 2iS\sqrt{\frac{\hbar}{2mN}}\sum_{\mathbf{k}s}\sum_{\mathbf{q}}\frac{M(\mathbf{k}s;\mathbf{q})}{\sqrt{\omega_s(\mathbf{k})}}\hat{A}(\mathbf{k}s)\hat{a}^{\dagger}_{\mathbf{k}+\mathbf{q}}\hat{a}_{\mathbf{q}}, \quad (11)$$

with $\hat{A}(\mathbf{k}s) = \hat{b}_{\mathbf{k}s} + \hat{b}^{\dagger}_{-\mathbf{k}s}$ and the amplitude

$$M(\mathbf{k}s;\mathbf{q}) = \sum_{\boldsymbol{\delta}}\left(\frac{1}{\delta}\frac{dJ}{d\delta}\right)(\mathbf{e}(\mathbf{k}s)\,\boldsymbol{\delta})(\mathbf{k}\,\boldsymbol{\delta})[1 - e^{i\mathbf{q}\boldsymbol{\delta}}], \quad (12)$$

where due account has been taken of the fact that the lattice possesses inversion symmetry. Note that the derivation of the magnon-phonon interaction (11) was based on the assumption that the ultrasonic wave frequency is usually of the order of 100 MHz. This means that the sound wave wavelength must be much larger δ, which is of the order of the lattice constant.

As $J(a)$ is assumed to be notably larger than $J(c)$, the strength of magnon-phonon coupling for ultrasonic propagation in the *ab* plane will be larger than for propagation along the *c* axis. This is readily seen from Eq. (12). For clarity, lattice vibrations propagating along the crystallographic direction [100] are chosen in the subsequent treatment.

III. EXCHANGE-MEDIATED MAGNON-PHONON INTERACTION

The phonon Green function determined in the Matsubara representation by $\mathcal{D}(\mathbf{k}s,\tau) = -\langle\hat{T}_\tau\hat{A}(\mathbf{k}s,\tau)\hat{A}(-\mathbf{k}s,0)\rangle$, where $\hat{T}_\tau$ is the imaginary time ordering operator with $-\beta \leqslant \tau \leqslant \beta$, gives the frequency-dependent form for bare phonons

$$\mathcal{D}^{(0)}(\mathbf{k}s, i\omega_n) = -\frac{2\omega_s(\mathbf{k})}{\omega_n^2 + \omega_s^2(\mathbf{k})}. \quad (13)$$

Here, $\omega_n = 2\pi n/\beta$ and $\beta = 1/k_BT$ is the inverse temperature.

Similarly, the magnon Green function defined by $\mathcal{G}(\mathbf{q},\tau) = -\langle\hat{T}_\tau\hat{a}_{\mathbf{q}}(\tau)\hat{a}^{\dagger}_{\mathbf{q}}(0)\rangle$ yields the noninteracting magnon Green function of Matsubara frequency

$$\mathcal{G}^{(0)}(\mathbf{q}, i\omega_n) = \frac{1}{i\omega_n - \varepsilon_{\mathbf{q}}}. \quad (14)$$

The general expression for phonon Green function, on account of the interaction with magnons, is determined by Dyson equation and given in the form

$$\mathcal{D}(\mathbf{k}s, i\omega_n) = \frac{\mathcal{D}^{(0)}(\mathbf{k}s, i\omega_n)}{1 - \mathcal{D}^{(0)}(\mathbf{k}s, i\omega_n)\Pi(\mathbf{k}s, i\omega_n)}. \quad (15)$$

The basic process contributing to the phonon self-energy Π is given by the magnon loop as shown in Fig. 2:

$$\Pi(\mathbf{k}s, i\omega_n) = \frac{2\hbar S^2}{mN}\sum_{\mathbf{q}}\frac{M(\mathbf{k}s;\mathbf{q})M(-\mathbf{k}s;\mathbf{k}+\mathbf{q})}{\omega_s(\mathbf{k})} \times \frac{1}{\beta}\sum_{p}\mathcal{G}^{(0)}(\mathbf{q}, i\omega_p)\mathcal{G}^{(0)}(\mathbf{k}+\mathbf{q}, i\omega_n + i\omega_p). \quad (16)$$

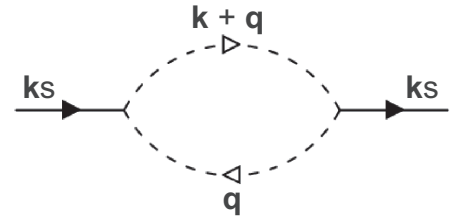

FIG. 2. Feynman diagram giving rise to the phonon self-energy in the lowest order. The solid lines represent phonon propagators while the dotted lines represent magnon propagators.

Performing the summation over the Matsubara frequencies, one gets eventually

$$\Pi(\mathbf{k}s, i\omega_n) = \frac{2\hbar S^2}{mN}\sum_{\mathbf{q}}\frac{M(\mathbf{k}s;\mathbf{q})M(-\mathbf{k}s;\mathbf{k}+\mathbf{q})}{\omega_s(\mathbf{k})} \times \frac{n_B(\varepsilon_{\mathbf{k}+\mathbf{q}}) - n_B(\varepsilon_{\mathbf{q}})}{\varepsilon_{\mathbf{q}} - \varepsilon_{\mathbf{k}+\mathbf{q}} + i\omega_n}, \quad (17)$$

where the symmetry of the phonon spectrum $\omega_s(-\mathbf{k}) = \omega_s(\mathbf{k})$ under inversion is accounted for. Here, $n_B(\varepsilon) = (e^{\beta\varepsilon} - 1)^{-1}$ is the Bose distribution function.

In ultrasonic attenuation experiments, the response of the lattice to a forced vibration of atom displacements at one end of the crystal is measured. The description of the task provided by the linear response theory leads to the basic result (see the Appendix)

$$\langle u_{i\alpha}\rangle_F(t) = -\frac{\hbar}{2mN}\sum_{i'\alpha'}\sum_{\mathbf{k}s}e^{i\mathbf{k}(\mathbf{R}_i - \mathbf{R}'_{i'})} \times \frac{\mathbf{e}_\alpha(\mathbf{k}s)\mathbf{e}_{\alpha'}(\mathbf{k}s)}{\omega_s(\mathbf{k})}\mathcal{D}_{\rm ret}(\mathbf{k}s, \omega_e)e^{-i\omega_e t}F_{i'\alpha'}. \quad (18)$$

Here, the force $F_{i'\alpha'}$ of the frequency ω_e generates sound waves in a crystal acting on ions at the lateral crystal surface, which are indexed by i' ($\alpha, \alpha' = x, y, z$).

The retarded phonon Green function at real frequencies that is involved in Eq. (18) may be found from Eq. (15) via the analytic continuation $i\omega_n \to \omega + i0^+$. This yields

$$\mathcal{D}_{\rm ret}(\mathbf{k}s, \omega_e) = \frac{2\omega_s(\mathbf{k})}{\omega_e^2 - \omega_s^2(\mathbf{k}) - 2\omega_s(\mathbf{k})\Pi_{\rm ret}(\mathbf{k}s, \omega_e)} \quad (19)$$

with $\Pi_{\rm ret}(\mathbf{k}s, \omega_e) = \Pi'_{\rm ret}(\mathbf{k}s, \omega_e) + i\Pi''_{\rm ret}(\mathbf{k}s, \omega_e)$. The positions of the complex poles in the expression are determined by

$$\omega_e^2 = \omega_s^2(\mathbf{k}) + 2\omega_s(\mathbf{k})\Pi_{\rm ret}(\mathbf{k}s, \omega_e). \quad (20)$$

To obtain final results, it is customary to consider the wave vector $\kappa_r(\omega_e)$ describing the propagation of the sound wave at frequency ω_e and the ultrasonic attenuation coefficient $\alpha_r(\omega_e)$

as the real and imaginary parts of the complex wave vector $k_r = \kappa_r + i\alpha_r$, respectively, where one need to consider those poles for which $\kappa_r \gg \alpha_r$.

Then, the real part of Eq. (20) leads to the implicit equation for $\kappa_r(\omega_e)$

$$\omega_e^2 \approx \omega_s^2(\kappa_r) + 2\omega_s(\kappa_r)\Pi'_{\rm ret}(\kappa_r s, \omega_e), \tag{21}$$

and the imaginary part gives the ultrasonic attenuation coefficient

$$\alpha_r(\omega_e) \approx -\Pi''_{\rm ret}(\kappa_r s, \omega_e)/(\partial\omega_s/\partial k)_{k=\kappa_r}. \tag{22}$$

IV. ULTRASOUND PROPAGATION

In trigonal crystals, to which $LuCo_3$ belongs to, the elastic energy density reads

$$\begin{aligned} U_e = {} & \tfrac{1}{2}c_{11}\left(u_{xx}^2 + u_{yy}^2\right) + c_{12}u_{xx}u_{yy} + \tfrac{1}{2}c_{33}u_{zz}^2 \\ & + c_{13}u_{zz}(u_{xx} + u_{yy}) + 2c_{14}u_{yz}(u_{xx} - u_{yy}) \\ & + (c_{11} - c_{12})u_{xy}^2 \\ & + 4c_{14}u_{xy}u_{xz} + 2c_{44}\left(u_{xz}^2 + u_{yz}^2\right), \end{aligned} \tag{23}$$

where c_{ij} are the elastic constants and the strain tensor is introduced

$$u_{ij} = \frac{1}{2}\left(\frac{\partial u_i}{\partial x_j} + \frac{\partial u_j}{\partial x_i}\right). \tag{24}$$

The vibrations of an elastic medium of density ρ are governed by the equation of motion $\rho\partial_t^2 u_i = \partial_k\sigma_{ik}$ with the stress tensor derived from the relation

$$\sigma_{ik} = \tfrac{1}{2}(1 + \delta_{ik})\partial U_e/\partial u_{ik}. \tag{25}$$

Writing out the equations of motion for the components u_i and substituting the periodic solution $u_i = u_i e^{i\mathbf{kr} - i\omega t}$ into these formulas, one obtains

$$\omega^2 u_\alpha = \sum_\beta D_{\alpha\beta}(\mathbf{k})u_\beta, \tag{26}$$

where the dynamical matrix is

$$D_{\alpha\beta}(\mathbf{k}) = \frac{1}{\rho}\begin{pmatrix} c_{11}k_x^2 + \frac{1}{2}(c_{11} - c_{12})k_y^2 + 2c_{14}k_yk_z + c_{44}k_z^2 & \frac{1}{2}(c_{11} + c_{12})k_xk_y + 2c_{14}k_xk_z & (c_{13} + c_{44})k_xk_z + 2c_{14}k_xk_y \\ \frac{1}{2}(c_{11} + c_{12})k_xk_y + 2c_{14}k_xk_z & c_{11}k_y^2 + \frac{1}{2}(c_{11} - c_{12})k_x^2 - 2c_{14}k_yk_z + c_{44}k_z^2 & c_{14}(k_x^2 - k_y^2) + (c_{13} + c_{44})k_yk_z \\ (c_{13} + c_{44})k_xk_z + 2c_{14}k_xk_y & c_{14}(k_x^2 - k_y^2) + (c_{13} + c_{44})k_yk_z & c_{44}(k_x^2 + k_y^2) + c_{33}k_z^2 \end{pmatrix}. \tag{27}$$

Using the notation $\omega^2(\mathbf{k}s)$ $(s = 1, 2, 3)$ for the eigenvalues of the dynamical matrix, the eigenvectors $\mathbf{e}(\mathbf{k}s)$ are derived from

$$\sum_\beta [D_{\alpha\beta}(\mathbf{k}) - \omega^2(\mathbf{k}s)\delta_{\alpha\beta}]e_\beta(\mathbf{k}s) = 0. \tag{28}$$

When eigenvectors are normalized, the relationship

$$\sum_\alpha e_\alpha^*(\mathbf{k}s)e_\alpha(\mathbf{k}s') = \delta_{ss'} \tag{29}$$

follows from their orthogonality, and

$$\sum_s e_\alpha^*(\mathbf{k}s)e_\beta(\mathbf{k}s) = \delta_{\alpha\beta}. \tag{30}$$

from their completeness.

The polarization dependence of different sound wave modes may be deduced from Eq. (27). For vibrations propagating along the direction [100] and characterized by the wave vector $\mathbf{k} = (k, 0, 0)$ there are the longitudinal wave with the spectrum

$$\omega_1(\mathbf{k}) = \sqrt{\frac{c_{11}}{\rho}}k \tag{31}$$

with polarization $\mathbf{e}(\mathbf{k}1) = (1, 0, 0)$, and two transverse branches

$$\omega_{2,3}(\mathbf{k}) = \frac{k}{\sqrt{2\rho}}\left\{\frac{1}{2}(c_{11} - c_{12}) + c_{44} \pm \sqrt{\left[\frac{1}{2}(c_{11} - c_{12}) - c_{44}\right]^2 + 4c_{14}^2}\right\}^{\frac{1}{2}}, \tag{32}$$

with the corresponding polarization vectors $\mathbf{e}(\mathbf{k}2) = (0, \epsilon_1, \epsilon_2)$, $\mathbf{e}(\mathbf{k}3) = (0, \epsilon_2, -\epsilon_1)$. Here,

$$\epsilon_{1,2} = \frac{1}{\sqrt{2}}\left[1 \pm \frac{1}{\sqrt{1 + \zeta^2}}\right]^{\frac{1}{2}}, \tag{33}$$

where $\zeta = 4c_{14}/(c_{11} - c_{12} - 2c_{44})$.

From now on, the question of ultrasound attenuation in $LuCo_3$ may be addressed. To be specific, we choose a crystal with trigonal symmetry and a free surface being the yz plane at $x = 0$. We start with the formula (18) for displacements generated by an external force and assume that the outer force is nonzero only when the cells i' lie on the surface plane and that it is identical in every cell. The analysis below is greatly simplified if another assumption is made, namely, the external force acts only along the x axis, $\alpha' = x$, and generates acoustic vibrational modes of the given wave vector $\mathbf{k} = (k, 0, 0)$. Then, it is not difficult to see that the transverse acoustic modes can be eliminated and the expression for the displacement of the cell located at the distance x_i from the surface plane takes the form

$$\langle u_{ix}\rangle_F(t) \propto -\frac{\hbar F_x}{mN_x}\sum_k \frac{\mathcal{D}_{\rm ret}(k1, \omega_e)}{\omega_1(k)}e^{ikx_i - i\omega_e t}. \tag{34}$$

Here, the the summation goes over all $\mathbf{k}$ points inside the first Brillouin zone (BZ), which lie on the x axis of the reciprocal lattice, N_x is the number of these points. This sum is restricted

to the range $-4\pi/3a < k < 4\pi/3a$ bearing in mind that the BZ of the trigonal system is specified by the primitive vectors $\mathbf{b}_1 = (2\pi/a)\{1, 1/\sqrt{3}, 0\}$, $\mathbf{b}_2 = (2\pi/a)\{0, 2/\sqrt{3}, 0\}$ and $\mathbf{b}_2 = (2\pi/c)\{0, 0, 1\}$.

Transforming the sum over k into an integral $\frac{1}{N_x}\sum_k \ldots \to \frac{3a}{8\pi}\int_{-\frac{4\pi}{3a}}^{\frac{4\pi}{3a}} dk \ldots$, one finally gets

$$\langle u_x\rangle_F \propto \int_{-\frac{4\pi}{3a}}^{\frac{4\pi}{3a}} dk \frac{e^{ikx - i\omega_e t}}{\omega_e^2 - \omega_1^2(k) - 2\omega_1(k)\Pi_{\rm ret}(k1, \omega_e)/\hbar}, \quad (34)$$

where all frequencies are taken in Hz units.

This integral can be performed by closing the contour of integration in the upper half-plane, so the displacement in the presence of a driving force behaves as $\langle u_x\rangle_F(x) \propto \sum_r \mathcal{Z}_r(\omega_e)\exp[i\kappa_r(\omega_e)x - \alpha_r(\omega_e)x]$, where the sum runs over the poles of the integrand. Here, $\kappa_r(\omega_e)$ and $\alpha_r(\omega_e)$ are the real and imaginary parts of the poles, and $\mathcal{Z}_r(\omega_e)$ are their residues.

To calculate κ_r, one may use Eq. (21), in which the real part of the self-energy is derived from Eq. (17) with $\mathbf{k} = (k, 0, 0)$

$$\Pi'_{\rm ret}(k1, \omega_e) = \frac{2\hbar S^2 V_{\rm cell}}{m\omega_1(k)} \fint_{\rm BZ} \frac{d\mathbf{q}}{(2\pi)^3} \times M(k1; \mathbf{q})M(-k1; k\mathbf{e}_x + \mathbf{q}) \times \frac{[n_B(\varepsilon_{k\mathbf{e}_x+\mathbf{q}}) - n_B(\varepsilon_{\mathbf{q}})]}{\varepsilon_{\mathbf{q}} - \varepsilon_{k\mathbf{e}_x+\mathbf{q}} + \hbar\omega_e}, \quad (35)$$

where $\fint$ denotes the principal value and $V_{\rm cell} = \sqrt{3}a^2c/2$ is the volume of the elementary cell.

From Eq. (22), one may find α_r with the aid of the imaginary part of the self-energy

$$\Pi''_{\rm ret}(k1, \omega_e) = -\frac{2\pi\hbar S^2 V_{\rm cell}}{m\omega_1(k)} \int_{\rm BZ} \frac{d\mathbf{q}}{(2\pi)^3} \times M(k1; \mathbf{q})M(-k1; k\mathbf{e}_x + \mathbf{q})[n_B(\varepsilon_{k\mathbf{e}_x+\mathbf{q}}) - n_B(\varepsilon_{\mathbf{q}})]\delta(\varepsilon_{\mathbf{q}} - \varepsilon_{k\mathbf{e}_x+\mathbf{q}} + \hbar\omega_e), \quad (36)$$

where $\delta(\ldots)$ is a Dirac delta function.

The amplitudes of magnon-phonon scattering are obtained from Eq. (12)

$$M(k1; \mathbf{q}) = kaJ'(a)\Big[3 - 2\cos(q_x a) - \cos\Big(\frac{q_x a}{2}\Big)\cos\Big(\frac{\sqrt{3}q_y a}{2}\Big)\Big], \quad (37)$$

and

$$M(-k1; k\mathbf{e}_x + \mathbf{q}) = -kaJ'(a)\Big[3 - 2\cos(q_x a) - \cos\Big(\frac{q_x a}{2}\Big)\cos\Big(\frac{\sqrt{3}q_y a}{2}\Big)\Big] - 2k^2a^2J'(a)\Big[\sin(q_x a) + \frac{1}{4}\sin\Big(\frac{q_x a}{2}\Big) \times \cos\Big(\frac{\sqrt{3}q_y a}{2}\Big)\Big]. \quad (38)$$

Here, the condition $ka \ll 1$ is taken into account in the last expression.

V. NUMERICAL RESULTS

Ultrasound dispersion is defined by Eq. (21) and yields the sound wave vector k with given frequency and magnetic moment. This expression includes the real part of the self-energy given by Eq. (35), which relates k with parameters of the magnetic subsystem, or more precisely, the field dependence of k is governed by the field variation of the magnetization.

To trace the connection, the relation (21) can be recast in the equivalent form

$$\frac{1}{\gamma}\Big(\frac{\omega_e^2}{k^2} - v_0^2\Big) = \mathcal{I}(\eta), \quad (39)$$

where $\gamma = [2aJ'(a)]^2/(m\hbar\omega_e)$ is the effective constant of spin-phonon interaction, and $v_0 = \omega_1(k)/k$ is the zeroth-order ultrasound velocity. Below we consider γ as a fitting parameter of the theory.

The integral

$$\mathcal{I}(\eta) = -S^2\frac{V_{\rm cell}}{(2\pi)^3}\fint_{\rm BZ} d\mathbf{q}\, \frac{[n_B(\varepsilon_{k\mathbf{e}_x+\mathbf{q}}) - n_B(\varepsilon_{\mathbf{q}})]}{1 - \eta\big[\sin(q_x a) + \sin\big(\frac{q_x a}{2}\big)\cos\big(\frac{\sqrt{3}q_y a}{2}\big)\big]}\Big\{3 - 2\cos(q_x a) - \cos\Big(\frac{q_x a}{2}\Big)\cos\Big(\frac{\sqrt{3}q_y a}{2}\Big)\Big\} \times \Big\{\Big[3 - 2\cos(q_x a) - \cos\Big(\frac{q_x a}{2}\Big)\cos\Big(\frac{\sqrt{3}q_y a}{2}\Big)\Big] + 2ka\Big[\sin(q_x a) + \frac{1}{4}\sin\Big(\frac{q_x a}{2}\Big)\cos\Big(\frac{\sqrt{3}q_y a}{2}\Big)\Big]\Big\} \quad (40)$$

with $\eta = 4SJ(a)ka/\hbar\omega_e$ depends on spin degrees of freedom.

The solution of Eq. (39) can be found graphically in the vicinity of the low-spin–high-spin crossover as indicated in Fig. 3. As seen from this plot, a propagating sound wave may split into three channels in this range of the magnetic fields, if the strength of the magnon-phonon coupling γ is strong enough.

The same conclusion is drawn from the calculated curve of the ultrasound wave vector k presented in Fig. 4. Apparently, the curve varies continuously with the magnetic field, however, the $k(H)$ dependence becomes three-valued in the vicinity of the low-spin–high-spin crossover, when γ is increased (see insets in Fig. 4). Given the frequency ω_e, the plot determines the inverse ultrasound velocity v as a function

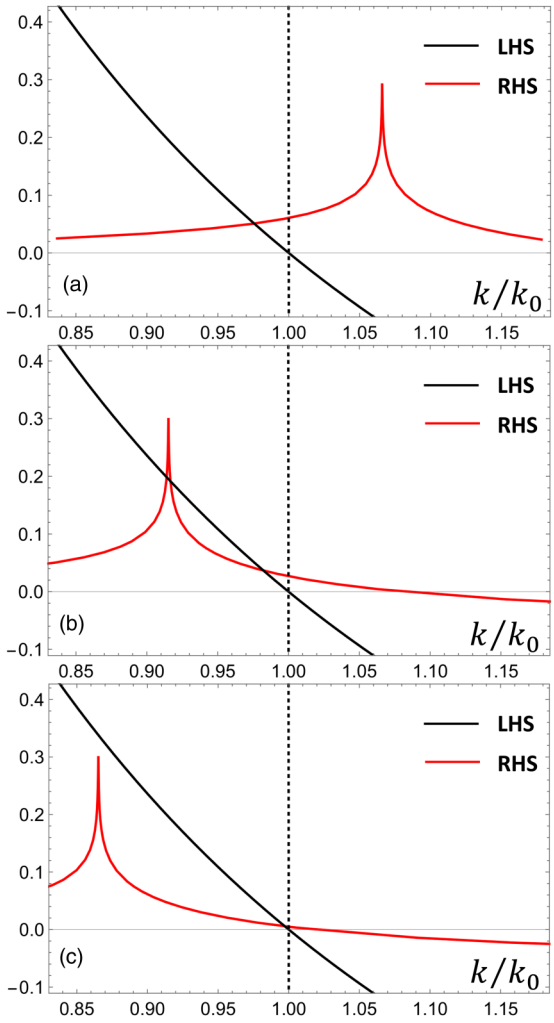

FIG. 3. Numerical evaluation of our result (39), where the left/right-hand side is shown by black/red curves, respectively, at (a) $H = 47.67\,T$; (b) $H = 48.49\,T$; (c) $H = 48.86\,T$. The black solid line corresponds to the strong magnon-phonon coupling ($\gamma/\pi^3 = 1.5 \times 10^7\,\mathrm{m^2\,s^{-2}}$), while the dotted line does to the weak coupling regime ($\gamma/\pi^3 = 1.0 \times 10^4\,\mathrm{m^2\,s^{-2}}$). The ultrasound frequency $\omega_e/2\pi = 2.6 \times 10^7$ Hz, and the velocity $v_0 = 3886$ m/s (or $k_0 = \omega_e/v_0 = 42.039 \times 10^3\,\mathrm{m^{-1}}$). The exchange coupling $J(a)/\mathrm{k}_B = 0.625$ K.

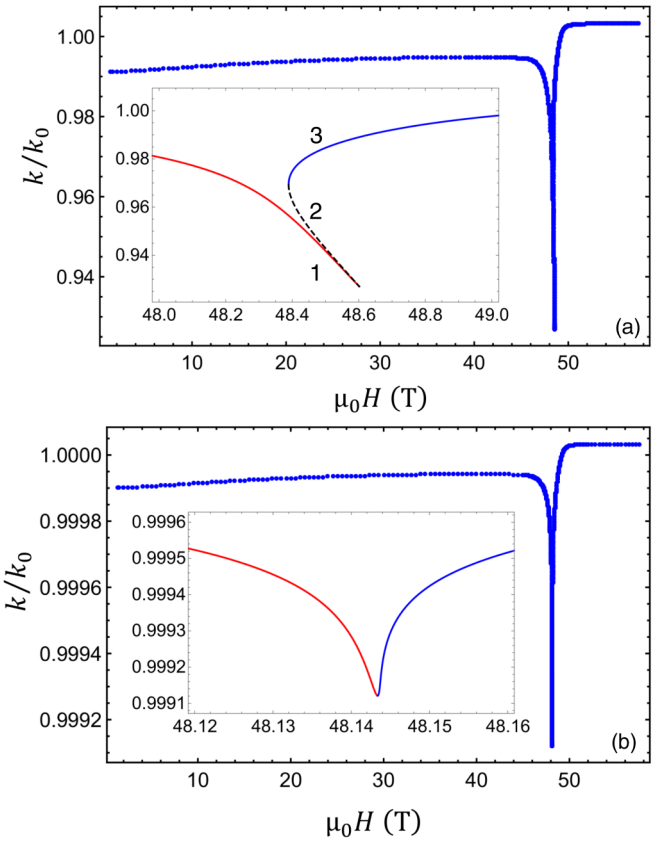

FIG. 4. Wave vector of the ultrasound mode propagating along the [100] axis measured in k_0 units as a function of the magnetic field directed along the [001] axis. The cases of (a) strong $\gamma/\pi^3 = 8.00 \times 10^6\,\mathrm{m^2\,s^{-2}}$ and (b) weak $\gamma/\pi^3 = 8.68 \times 10^4\,\mathrm{m^2\,s^{-2}}$ magnon-phonon interaction are shown. The $k(H)$ behavior near the low-spin-high-spin crossover is zoomed in insets, where three branches are marked by 1 (red solid), 2 (black dashed) and 3 (blue solid). The exchange coupling $J(a) = 0.6095\,\mathrm{k}_B$, the wave vector $k_0 = 42.039 \times 10^3\,\mathrm{m^{-1}}$.

of H. Consequently, one may expect a smooth decrease of v with increasing H below the crossover, followed by a sharp growth in the transition region, then succeeded by a drop of velocity to values less than they were at low H. It must be emphasized that this behavior of ultrasound velocity is due to dynamical magnon-phonon scattering process. However, static coupling of strain deformations with electronic degrees of freedom, which is highly sensible to the low-spin–high-spin crossover, may result in a strong effect on elastic constants and take precedence in sound velocity changes.

As the crossover field is reached, ultrasound attenuation illustrated in Fig. 5 exhibits a sharp growth then succeeded by monotonic decreasing. Significantly, enhancement of magnon-phonon coupling provides additional channels for ultrasound propagation in the crossover region.

A drastic modification of the ultrasound propagation in the ferromagnetic specimen in the increasing magnetic field is directly linked to a change in the nature of magnon-phonon scattering process due to the low-spin-high-spin transition. This variation is stipulated by the field dependence of the phonon self-energy, which may be traced with the aid of Eqs. (17) and (40).

The key parameter is η, which determines whether $\Pi_{\mathrm{ret}}(k1, \omega_e)$ contains a singularity or not. This divergency arises from the poles of the polarization bubble for which $\varepsilon_{k\mathbf{e}_x+\mathbf{q}} = \varepsilon_{\mathbf{q}} + \hbar\omega_e$. From the expression (40) it is readily seen that there is the threshold value

$$\eta_{\mathrm{crit}} = \frac{32}{(3+\sqrt{33})\sqrt{30+2\sqrt{33}}} \approx 0.568, \qquad (41)$$

below which the off-resonant magnon-phonon interaction results in the anharmonic correction to the sound phonon dispersion relation [53] $\omega_e^2 = v_0^2 k^2 + \Delta k^4$, where the positive

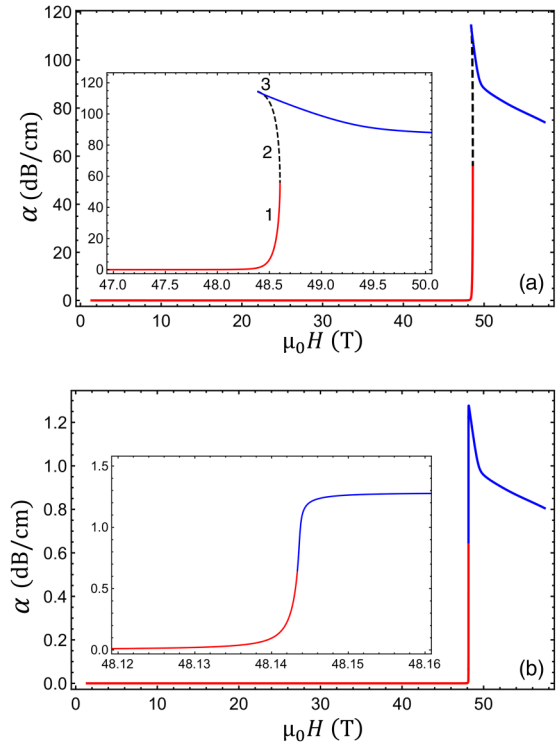

FIG. 5. Attenuation coefficient α with respect to the magnetic field for the ultrasonic wave propagating along the [100] axis. The regimes of the strong (a) $\gamma/\pi^3 = 8.00 \times 10^6\,\mathrm{m^2\,s^{-2}}$ and (b) the weak $\gamma/\pi^3 = 8.68 \times 10^4\,\mathrm{m^2\,s^{-2}}$ magnon-phonon interaction are presented. The other parameters are the same as in Fig. 4. (a) Inset: attenuation becomes multivalued near the low-spin–high-spin crossover with three branches: 1 (red solid), 2 (black dashed) and 3 (blue solid). (b) Inset: attenuation remains a smooth, single-valued function in the crossover region.

parameter is introduced

$$\Delta \approx \gamma(4Sa)^2\left(\frac{J(a)S}{k_BT}\right)\frac{V_{\mathrm{cell}}}{(2\pi)^3}\int_{\mathrm{BZ}} d\mathbf{q}\,\frac{\sin^2\left(\frac{q_xa}{2}\right)}{4\sinh^2\left(\frac{\varepsilon_{\mathbf{q}}}{2k_BT}\right)} \times\left[A_1(\mathbf{q}_\perp)A_2(\mathbf{q}_\perp)A_3(\mathbf{q}_\perp)+\frac{J(a)S}{\hbar\omega_e}A_1^2(\mathbf{q}_\perp)A_3^2(\mathbf{q}_\perp)\right] \tag{42}$$

with

$$A_1(\mathbf{q}_\perp) = 3 - 2\cos(q_xa) - \cos\left(\frac{q_xa}{2}\right)\cos\left(\frac{\sqrt{3}q_ya}{2}\right),$$

$$A_2(\mathbf{q}_\perp) = \cos\left(\frac{q_xa}{2}\right) + \frac{1}{8}\cos\left(\frac{\sqrt{3}q_ya}{2}\right),$$

$$A_3(\mathbf{q}_\perp) = 2\cos\left(\frac{q_xa}{2}\right) + \cos\left(\frac{\sqrt{3}q_ya}{2}\right).$$

Above the threshold value, $\eta = 4SJ(a)ka/\hbar\omega_e > \eta_{\mathrm{crit}}$, the resonant mechanism becomes relevant, when scattered magnons directly gain energy due to phonon energy losses. For fixed values of ultrasound frequency ω_e, the spin moment S is the only parameter which can be effectively controlled by the applied field, as long as the sound wave vector k is not significantly changed. This explains the dramatic increase of ultrasound attenuation as the field approaches the crossover point.

The behavior of the wave vector k with increasing H is also governed by the field dependence of the phonon self-energy. When H is less than the crossover field it affects $\Pi_{\mathrm{ret}}(k1, \omega_e)$ mostly through the thermal population of magnon states. As a consequence, contribution of the magnon-phonon interaction to the phonon dispersion relation turns out to be appreciably suppressed, which is manifested through the tendency $k/k_0 \to 1$ as the field increases. However, the situation is drastically altered in the crossover region, when the phonon self-energy depends crucially on the spin value, namely, $\Pi_{\mathrm{ret}}(k1, \omega_e)$ starts to grow linearly with S that leads to the noticeable dip in the wave vector curve around the crossover point (see Fig. 3).

The attenuation coefficient determined from measurements is defined as the weighted average of $\alpha(\mathbf{k}, \omega)$ distributed generally continuously over the allowed $\mathbf{k}$ vectors. The spectral density function

$$B(\mathbf{k}s, \omega) = -2\mathrm{Im}\mathcal{D}_{\mathrm{ret}}(\mathbf{k}s, \omega) \tag{43}$$

provides the proper probability weighting between the momentum and the energy of phonons.

Given the ultrasound frequency ω_e, the averaged attenuation coefficient can be determined from

$$\bar{\alpha}_s(\omega_e) = \frac{\int d\mathbf{k}B(\mathbf{k}s, \omega_e)\alpha_s(\mathbf{k}, \omega_e)}{\int d\mathbf{k}B(\mathbf{k}s, \omega_e)}. \tag{44}$$

In our case, the sound wave may propagate through the specimen in a finite number of channels N_r specified by Eqs. (21) and (22). The spectral density of the channel with the wave vector κ_r and attenuation α_r is found to be

$$B(\kappa_r, \omega_e) = \frac{2}{\alpha_r(\omega_e)[\partial\omega_1/\partial k]_{k=\kappa_r}} \approx \frac{2}{\alpha_r(\omega_e)v_0}. \tag{45}$$

Then, the weighted average of attenuation is given by

$$\bar{\alpha}(\omega_e) = \frac{\sum_r B(\kappa_r, \omega_e)\alpha_r(\omega_e)}{\sum_r B(\kappa_r, \omega_e)} \approx \frac{N_r}{\sum_r[\alpha_r(\omega_e)]^{-1}}. \tag{46}$$

The function $\bar{\alpha}(\omega_e)$ is plotted against the magnetic field in Fig. 6. Note that it features finite jumps at 48.4 and 48.6 T, i.e., at the beginning and at the end of the ultrasound multichannel regime. An experimental observation of these singularities may give a direct detection of phonon energy absorption by the spin system through several channels in the vicinity of the low-spin–high-spin crossover.

The field dependences of k and $\bar{\alpha}$ measured at various temperatures are presented in Fig. 7. At low temperatures excitation of magnons is dominated by their occupation number, which can be neglected, and we are dealing with nearly free propagation of phonons without scattering process. When temperature is increased even further, this tendency is counterbalanced by the rapid increase in magnetization due to the low-spin–high-spin crossover. This makes the magnon-phonon interaction effectively stronger and the inelastic magnon-phonon processes come into play, what is manifested in the results for $T = 80\,\mathrm{K}$. At sufficiently high temperature, an even more interesting situation occurs, when magnetization reaches saturation at fields beyond the highest field achieved in the experiment (~60 T) [12]. As seen

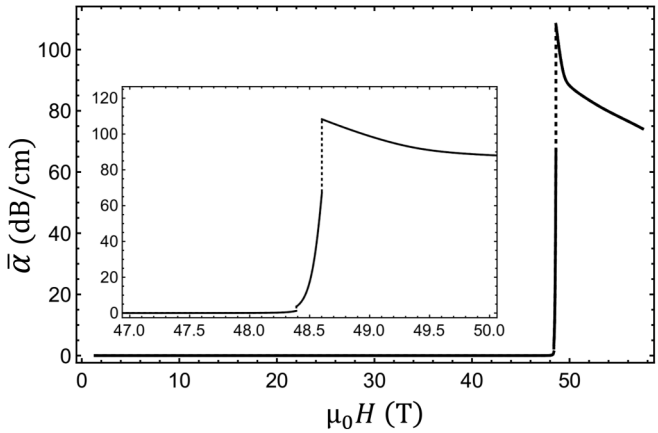

FIG. 6. The field dependence of the averaged ultrasound attenuation for the strong magnon-phonon coupling $\gamma/\pi^3 = 8.00 \times 10^6\,\mathrm{m^2\,s^{-2}}$ (the other parameters are the same as in Fig. 4). One can clearly see discontinuous jumps (dotted lines) when the transitions between single-channel and multi-channel regimes of phonon energy absorption occurs.

in Fig. 7(a), the multichannel regime of the propagation of phonons becomes extended over a broader field range, so there is no chance for return to a single sound wave regime for the fields in question. As a result, the shift of the peak in $\bar{\alpha}$ could be misinterpreted as a fall of ultrasound attenuation with increasing T [see data in Fig. 7(b) for 180 K]. The averaging procedure results in the effect like that of in a parallel resistor

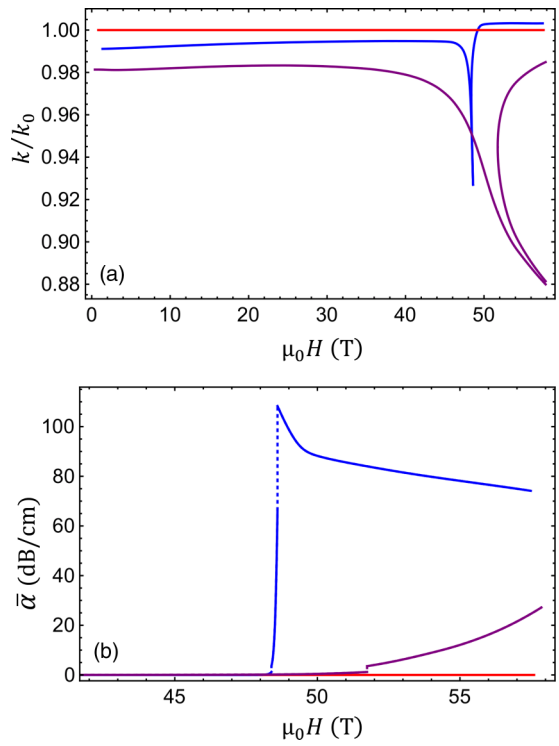

FIG. 7. Field evolution of (a) the ultrasound wave vector and (b) the averaged ultrasound attenuation at different temperatures: $T = 2\,\mathrm{K}$ (red line), $T = 80\,\mathrm{K}$ (blue line), and $T = 160\,\mathrm{K}$ (purple line). The parameters are taken as in Fig. 6.

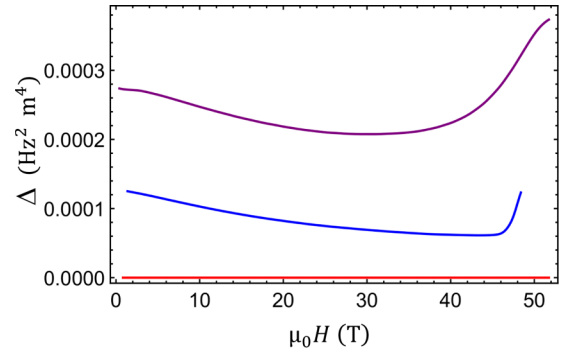

FIG. 8. The parameter of anharmonicity plotted against magnetic field at different temperatures: $T = 2\,\mathrm{K}$ (red line), $T = 80\,\mathrm{K}$ (blue line), and $T = 160\,\mathrm{K}$ (purple line). The curves are calculated below the point, where the multichannel regime appears. The parameters are taken as in Fig. 6.

circuit, namely, the averaged attenuation of a sample is determined by a channel with the smallest attenuation.

Finally, the field dependence of the anharmonicity parameter is given in Fig. 8. Apart from low temperatures, when magnon excitations are suppressed, Δ initially demonstrates a smooth decrease with increasing H, followed by a growth as a threshold to the multichannel regime of ultrasound propagation is approached.

VI. CONCLUSIONS

In summary, we discuss the possibility of experimental observation of the anomalous ultrasonic attenuation in the ferromagnet $LuCo_3$ near the low-spin–high-spin crossover triggered by the external high magnetic field. This crossover is not accompanied by the breaking of some symmetry and the character of spin excitations is left unchanged. Moreover, the completely different frequency ranges of the ultrasound and spin waves, MHz rather than THz, exclude any hybridization between them altogether. Despite the circumstances, we argue that ultrasound propagation may cause transitions between states of the magnon band associated with absorption of phonons. In our theory, we demonstrate that probability of the process is particularly sensitive to the value of magnetization, and as such, the external magnetic field acts as a switch between the off-resonant and resonant modes of ultrasound propagation.

Our analysis considers the experimental situation relevant for $LuCo_3$, which may result in enhanced ultrasonic attenuation and dramatic modification of the phonon dispersion relation, when the excited acoustic wave propagates perpendicularly to the easy magnetization direction. To model the magnetic part of interactions, $LuCo_3$ is regarded as a hard ferromagnetic material, where easy-axis anisotropy is highly strong. Coupling between lattice vibrations and spin moments is discussed in the framework of the exchange striction mechanism. The low-order perturbative treatment of the magnon-phonon interaction based on the diagram technique gives the self-energy corrections to the ultrasonic dispersion relation and attenuation. The criterion for the threshold of resonant phonon absorption, determined from a singularity

of the self-energy, highlights clearly a decisive role of the magnetization value.

Numerical solution of the equations specifying the field and temperature dependences of the ultrasonic wave number and attenuation show no changes in these quantities at low temperatures since magnetic fluctuations are drastically suppressed. However, such modifications become visible with increasing temperature and reflect different character of ultrasound propagation before and after the jump of magnetization. For the low-spin state, the magnon-phonon interaction gives rise to anharmonic corrections to the phonon dispersion relation, a modest increase in the ultrasonic wave number (or, equivalently, a decrease in velocity) and no attenuation. The high-spin state is characterized by pronounced scattering processes between magnons and phonons leading to a significant nonzero attenuation and to a slight reduction of ultrasonic velocity. We found that the most interesting effect occurs within the crossover region, when three independent channels of ultrasound propagation open in a certain magnetic field. A real experiment, however, will probe ultrasonic characteristics averaged over these channels with the aid of the phonon spectral density function.

Thus, in our approach anomalies of ultrasound attenuation and velocity variations arise from the interaction of acoustic phonons with thermally excited magnons that makes this mechanism effective at intermediate temperatures. On the other hand, ultrasound propagation may cause a rearrangement of the density of the Co $3d$ states near the Fermi level, which will be accompanied by noticeable fluctuations of a magnitude of the spin moment like those involved to describe ultrasound absorption near magnetic phase transitions [33]. Apparently, this mechanism will be relevant for the low temperature regime. In addition, there is a possibility of a structural phase transition triggered by the low-spin-high-spin crossover due to magnetoelastic coupling. Such a transition will have a deep impact on ultrasound velocity. Future experimental verification based on the pulse-echo phase-sensitive detection technique [13,18] is planned to get material insight on the issue.

ACKNOWLEDGMENTS

We acknowledge the support of HLD at HZDR, a member of European Magnetic Field Laboratory (EMFL). The research funding from the Ministry of Science and Higher Education of the Russian Federation (Ural Federal University Program of Development within the Priority-2030 Program) is gratefully acknowledged. A.S.O. acknowledges financial support by the Ministry of Science and Higher Education of the Russian Federation, Project No. FEUZ-2020-0054. A.A.T. acknowledges funding by the Foundation for the Advancement of Theoretical Physics and Mathematics BASIS Grant No. 21-1-5-149-1.

APPENDIX: LINEAR RESPONSE

According to linear response theory the displacement of the ith cell in the α direction caused by a weak external perturbation with the Hamiltonian $\mathcal{H}_1$ reads as

$$\langle u_{i\alpha}\rangle(t) = -\frac{i}{\hbar}\int_{-\infty}^{t} dt' \langle [u_{i\alpha}(t), \mathcal{H}_1(t')]\rangle_0, \tag{A1}$$

where the perturbation describes an external force $F_{i\alpha}(t)$ coupled linearly to the lattice displacements

$$\mathcal{H}_1(t) = -\sum_{i\alpha} u_{i\alpha} F_{i\alpha}(t). \tag{A2}$$

Then

$$\langle u_{i\alpha}\rangle_F(t) = \frac{i}{\hbar}\sum_{i',\alpha'}\int_{-\infty}^{\infty} dt' \theta(t-t')\langle [u_{i\alpha}(t), u_{i'\alpha'}(t')]\rangle_0 F_{i'\alpha'}(t'),$$

where $\theta(\ldots)$ is the Heaviside step function.

Using expression (8) for the lattice displacements in terms of the phonon creation and annihilation operators, one gets

$$\langle u_{i\alpha}\rangle_F(t) = -\frac{\hbar}{2mN}\sum_{i',\alpha'}\sum_{\mathbf{k}s} e^{i\mathbf{k}(\mathbf{R}_i-\mathbf{R}_{i'})}\frac{\mathbf{e}_\alpha(\mathbf{k}s)\mathbf{e}_{\alpha'}(\mathbf{k}s)}{\omega_s(\mathbf{k})}$$

$$\times \int_{-\infty}^{\infty} dt' \mathcal{D}_{\rm ret}(\mathbf{k}s, t-t') F_{i'\alpha'}(t'), \tag{A3}$$

on account of the inversion symmetry, which gives $\omega_s(-\mathbf{k}) = \omega_s(\mathbf{k})$ and $\mathbf{e}_\alpha(-\mathbf{k}s) = \mathbf{e}_\alpha(\mathbf{k}s)$. Here, the retarded Green function for phonons is defined through

$$D_{\rm ret}(\mathbf{k}s, t-t') = -\frac{i}{\hbar}\theta(t-t')\langle [\hat{A}_{\mathbf{k}s}(t), \hat{A}_{-\mathbf{k}s}(t')]\rangle. \tag{A4}$$

Introducing its temporal Fourier transform

$$D_{\rm ret}(\mathbf{k}s, t-t') = \int_{-\infty}^{\infty}\frac{d\omega}{2\pi} e^{-i\omega(t-t')}\mathcal{D}_{\rm ret}(\mathbf{k}s, \omega), \tag{A5}$$

and assuming that a harmonic force $F_{i'\alpha'}(t) = F_{i'\alpha'}e^{-i\omega_e t}$ is applied, Eq. (18) is recovered from Eq. (A3).

[1] K. Strnat, G. Hoffer, J. Olson, W. Ostertag, and J. J. Becker, A family of new cobalt-base prmanent magnet materials, J. Appl. Phys. **38**, 1001 (1967).

[2] J. Croat, J. F. Herbst, R. W. Lee, and F. E. Pinkerton, High-energy product Nd-Fe-B permanent magnets, J. Appl. Phys. **55**, 2078 (1984).

[3] M. Sagawa, S. Fujimura, M. Togawa, and Y. Matsuura, Magnetic properties of rare-earth-iron-boron permanent magnet materials, J. Appl. Phys. **55**, 2083 (1984).

[4] J. J. M. Franse and R. J. Radwański, in *Handbook of Magnetic Materials*, edited by K. H. J. Buschow (Elsevier, Amsterdam, 1993), Vol. 7, p. 307.

[5] J. J. M. Franse, F. E. Kayzel, C. Marquina, R. J. Radwanski, and R. Verhoef, High field magnetization of R_2T_{17} compounds, J. Alloys Compd. **181**, 95 (1992).

[6] Y. Skourski, M. D. Kuz'min, K. P. Skokov, A. V. Andreev, and J. Wosnitza, High-field magnetization of Ho_2Fe_{17}, Phys. Rev. B **83**, 214420 (2011).

[7] O. Isnard, A. V. Andreev, M. D. Kuz'min, Y. Skourski, D. I. Gorbunov, J. Wosnitza, N. V. Kudrevatykh, A. Iwasa, A. Kondo, A. Matsuo, and K. Kindo, High magnetic field study of the Tm_2Fe_{17} and $Tm_2Fe_{17}D_{3.2}$ compounds, Phys. Rev. B **88**, 174406 (2013).

[8] D. I. Gorbunov, C. Strohm, S. M. Henriques, P. van der Linden, B. Pedersen,V. N. Mushnikov, E. V. Rosenfeld, V. Petříček, O. Mathon, J. Wosnitza, and V. A. Andreev, Microscopic Nature of the First-Order Field-Induced Phase Transition in the Strongly Anisotropic Ferrimagnet $HoFe_5Al_7$, Phys. Rev. Lett. **122**, 127205 (2019).

[9] M. D. Kuz'min, Y. Skourski, K. P. Skokov, and K.-H. Müller, High-field magnetization measurements on Er_2Fe_{17} single crystals, Phys. Rev. B **75**, 184439 (2007).

[10] M. D. Kuz'min, High-field low-temperature magnetization curves of anisotropic ferrimagnets, J. Magn. Magn. Mater. **323**, 1068 (2011).

[11] D. I. Gorbunov, A. V. Andreev, Y. Skourski, and M. D. Kuz'min, High-field magnetization of a $DyFe_5Al_7$ single crystal, J. Alloys Compd. **553**, 358 (2013).

[12] D. S. Neznakhin, D. I. Radzivonchik, D. I. Gorbunov, A. V. Andreev, J. Šebek, A. V. Lukoyanov, and M. I. Bartashevich, Itinerant metamagnetic transition in the ferromagnet $LuCo_3$ induced by high field: Instability of the 3d-electron subsystem, Phys. Rev. B **101**, 224432 (2020).

[13] B. Lüthi, *Physical Acoustics in the Solid States* (Springer, Berlin, 2007).

[14] G. Leisure, *Ultrasonic Spectroscopy: Application in Condensed Matter Physics and Material Science* (Cambridge University Press, Cambridge, 2017).

[15] S. Maekawa, R. A. Treder, M. Tachiki, M. C. Lee, and M. Levy, Ultrasonic study of terbium in a magnetic field, Phys. Rev. B **13**, 1284 (1976).

[16] S. Kusaka, K. Yamamoto, T. Komatsubara, and Y. Ishikawa, Ultrasonic study of magnetic phase diagram of MnSi, Solid State Commun. **20**, 925 (1976).

[17] J. Takeuchi, T. Ito, and M. Oka, Ultrasonic study of a single crystal $Gd_{70}Y_{20}Lu_{10}$ alloy in a magnetic field, J. Phys. Soc. Jpn. **54**, 3076 (1985).

[18] S. Zherlitsyn, S. Yasin, J. Wosnitza, A. A. Zvyagin, A. V. Andreev, and V. Tsurkan, Spin-lattice effects in selected antiferromagnetic materials (Review Article), Low Temp. Phys. **40**, 123 (2014).

[19] M. Michelmann, V. Moshnyaga, and K. Samwer, Colossal magnetoelastic effects at the phase transition of $(La_{0.6}Pr_{0.4})_{0.7}Ca_{0.3}MnO_3$, Phys. Rev. B **85**, 014424 (2012).

[20] G. Gorodetsky and B. Lüthi, Sound-wave–soft-mode interaction near displacive phase pransitions: Spin reorientation in ErFe, Phys. Rev. B **2**, 3688 (1970).

[21] G. Gorodetsky, S. Shaft, and B. M. Wanklyn, Magnetoeiastic properties of $TmFe0_3$ a at the spin reorientation region, Phys. Rev. B **14**, 2051 (1976).

[22] C. D. Fuerst, J. F. Herbst, J. L. Sarrao, and A. Migliori, Resonant ultrasound measurements of elastic constants in melt-spun $R_2Fe_{14}B$ compounds (R = Ce, Pr, Nd, Er), J. Appl. Phys. **75**, 6625 (1994).

[23] J. E. Bidaux and B. Cao, Elastic behaviour of pure cobalt near the spin reorientation phase transition, J. Phys.: Condens. Matter **3**, 2263 (1991).

[24] C. Patterson, D. Givord, J. Voiron, and S. B. Palmer, Magnetoelastic effects in the spin reorientation region of single crystal $NdCo_5$, J. Magn. Magn. Mater. **54-57**, Part 2, 891 (1986).

[25] N. K. Dan'shin, S. V. Zherlitsyn, S. S. Zvada, G. G. Kramarchuk, M. A. Sdvizhkov, and V. D. Fil', Dynamic properties of $YbFeO_3$ in the vicinity of an orientational phase transition, JETP **66**, 1227 (1987).

[26] D. I. Gorbunov, S. Yasin, A. V. Andreev, N. V. Mushnikov, E. V. Rosenfeld, Y. Skourski, S. Zherlitsyn, and J. Wosnitza, Phase transitions of anisotropic and exchange origins in $TmFe_5Al_7$, Phys. Rev. B **89**, 214417 (2014).

[27] A. V. Andreev, A. A. Zvyagin, Y. Skourski, S. Yasin, and S. Zherlitsyn, High-field magnetoelasticity of Tm_2Co_{17} and comparison with Er_2Co_{17}, Low Temp. Phys. **43**, 1254 (2017).

[28] A. V. Andreev, D. I. Gorbunov, T. Nomura, A. A. Zvyagin, G. A. Zvyagina, and S. Zherlitsyn, High-field magnetoacoustics of a $Dy_2Fe_{14}Si_3$ single crystal, J. Alloys Compd. **835**, 155335 (2020).

[29] T. Goto, H. A. Katori, T. Sakakibara, and M. Yamaguchi, Successive phase transitions in ferromagnetic YCo_3, Phys. B **177**, 255 (1992).

[30] M. I. Bartashevich, T. Goto, and K. Koui, Itinerant electron metamagnetism and magnetic anisotropy in the $Y(Co_{1-x}Fe_x)_3$ system, Phys. B **292**, 9 (2000).

[31] D. Koudela, U. Schwarz, H. Rosner, U. Burkhardt, A. Handstein, M. Hanfland, M. D. Kuz'min, I. Opahle, K. Koepernik, K.-H. Müller, and M. Richter, Magnetic and elastic properties of YCo_5 and $LaCo_5$ under pressure, Phys. Rev. B **77**, 024411 (2008).

[32] H. Yamaoka, Y. Yamamoto, E. F. Schwier, N. Tsujii, M. Yoshida, Y. Ohta, H. Sakurai, J.-F. Lin, N. Hiraoka, H. Ishii, K.-D. Tsuei, M. Arita, K. Shimada, and J. Mizuki, Pressure-induced phase transition in $LaCo_5$ studied by x-ray emission spectroscopy, x-ray diffraction, and density functional theory, Phys. Rev. B **94**, 165156 (2016).

[33] M. Tachiki and S. Maekawa, Effect of magnetic field on sound propagation near magnetic phase transition temperatures, Prog. Theor. Phys. **51**, 1 (1974).

[34] D. T. Vigren, Rare-Earth Ultrasonic Attenuation in Applied Fields, Phys. Rev. Lett. **38**, 1155 (1977).

[35] I. K. Kamilov and K. K. Aliev, Ultrasonic studies of the critical dynamics of magnetically ordered crystals, Phys. Usp. **41**, 865 (1998).

[36] K. Balakrishnan and S. N. Kaul, Determination of susceptibility and specific heat critical exponents for weak itinerant-electron ferromagnets from vibrating reed experiments, Phys. Rev. B **65**, 134412 (2002).

[37] P. V. Prudnikov and V. V. Prudnikov, Influence of long-range correlated defects on critical ultrasound propagation in solids, Phys. Rev. B **80**, 024115 (2009).

[38] C. Kittel, Interaction of spin waves and ultrasonic waves in ferromagnetic crystals, Phys. Rev. **110**, 836 (1958).

[39] V. D. Buchel'nikov, N. K. Dan'shin, L. T. Tsymbal, and V. G. Shavrov, Magnetoacoustics of rare-earth orthoferrites, Phys. Usp. **39**, 547 (1996).

[40] P. C. Kwok, Green's function method in lattice dynamics, in *Solid State Physics*, edited by F. Seitz and D. Turnbull, (Academic Press, New York, 1968), Vol. 20.

[41] G. Mahan, *Many-Particle Physics* (Plenum, New York, 1990).

[42] A. Rückriegel, P. Kopietz, D. A. Bozhko, A. A. Serga, and B. Hillebrands, Magnetoelastic modes and lifetime of magnons in thin yttrium iron garnet films, Phys. Rev. B **89**, 184413 (2014).

[43] S. Streib, N. Vidal-Silva, K. Shen, and G. E. W. Bauer, Magnon-phonon interactions in magnetic insulators, Phys. Rev. B **99**, 184442 (2019).

[44] R. Schmidt, F. Wilken, T. S. Nunner, and P. W. Brouwer, Boltzmann approach to the longitudinal spin Seebeck effect, Phys. Rev. B **98**, 134421 (2018).

[45] H. Stern, Thermal conductivity at the magnetic transition, J. Phys. Chem. Solids **26**, 153 (1965).

[46] C. Cazorla, O. Diéguez, and J. Íñiguez, Multiple structural transitions driven by spin-phonon couplings in a perovskite oxide, Sci. Adv. **3**, e1700288 (2017).

[47] See Supplemental Material at http://link.aps.org/supplemental/10.1103/PhysRevB.106.054417 for field dependences of the saturation magnetization at different temperatures.

[48] J. M. Coey, *Magnetism and Magnetic Materials* (Cambridge University Press, Cambridge, 2010).

[49] G. Gorodetsky, A. Shaulov, V. Volterra, and J. Makovsky, Strain-ion coupling effects on elastic constants of $FeCl_2$, Phys. Rev. B **13**, 1205 (1976).

[50] P. Morin and D. Schmitt, in *Handbook of Ferromagnetic Materials*, edited by K. H. J. Buschow and E. P. Wohlfarth (North-Holland, Amsterdam, 1990), Vol. 5.

[51] D. I. Radzivonchik, D. S. Neznakhin, and A. V. Lukoyanov, Spin-selective spin transition in $LuCo_3$, J. Phys. Chem. Solids **163**, 110552 (2022).

[52] K. P. Sinha and U. N. Upadhyaya, Phonon-magnon interaction in magnetic crystals, Phys. Rev. **127**, 432 (1962).

[53] J. A. Reissland, *Physics of Phonons* (Wiley, London, 1973).